$Ni_{0.4}Cu_{0.2}Zn_{0.4}Fe_2O_4$ Nanoferrite: Synthesis, Characterization, and Photocatalytic Application

K. D. Badave[1,2], S. R. Thopate[2]*

1 Department of Chemistry, Chandmal Tarachand Bora College of Arts, Commerce and Science, Shirur, Pune, 412210 (MS), India

2* Department of Chemistry, Radhabai Kale Mahila Mahavidyalaya of Arts, Commerce and Science, Ahilyanagar, 414001 (MS), India

*Email: srthopate@gmail.com

Received: 30.8.2026, Revised: 25.10.2026 Accepted: 26.10.2026

Abstract

$Ni_{0.4}Cu_{0.2}Zn_{0.4}Fe_2O_4$ nanoferrite was successfully synthesized via a citric acid-assisted sol-gel method, producing homogeneous and phase-pure spinel nanostructures. XRD confirmed the formation of a single-phase cubic spinel structure, while SEM and HRTEM revealed uniformly distributed nanoparticles with size ranging from 12 to 36 nm. FTIR spectra verified the characteristic spinel ferrite vibration and cation distribution in tetrahedral and octahedral site. UV-Vis. analysis showed direct and indirect band gap of 2.14 and 1.63 eV respectively, confirming the semiconducting nature of the material. EDS confirmed the elemental composition, and VSM measurement indicated ferromagnetic behavior with a saturation magnetization of 34.76 $emu.g^{-1}$ and high coercivity of 6.438 kOe. The synthesized nanoferrite exhibited excellent photocatalytic activity toward Congo red degradation and maintained stable performance over five reuse cycle. These results demonstrate its potential as an efficient, magnetically recoverable, and reusable photocatalyst for the remediation of dye-contaminated industrial wastewater.

Key words: spinel, ferrite, sol-gel, congo red, photocatalysis

1. Introduction

Spinel ferrite is a class of magnetic oxides with the general formula MFe_2O_4 (where M is a divalent metal ion), characterized by their high electrical resistivity, low eddy current losses, and chemical stability. These attributes render them highly desirable for a diverse range of technological, industrial, and environmental applications. Due to their tunable magnetic and electromagnetic properties allow for precise performance optimization in both high-frequency devices and catalytic systems[1,2]. Among these, Ni–Cu–Zn ferrite has garnered extensive attention

 DOI: 10.59143/isas.jisas.5.2.MFTR8070

for their versatile applications in multilayer chip inductors, magnetic sensors, and high-frequency devices, owing to their low sintering temperatures and favorable electromagnetic properties [2]. Beyond these applications, the magnetic nature, high surface area, and absorptivity of ferrite material, including those containing zinc and cobalt, also make them promising candidate for environmental remediation, particularly in photocatalytic degradation processes[3]. Their tunable band gap further enhances their utility as photocatalyst, enabling efficient degradation of organic pollutant under various light conditions[4,5]. Specifically, ternary ferrite such as Ni-Zn ferrite and Ni-Zn-Cu ferrite have demonstrated efficacy in photocatalytic degradation of organic dyes, attributable to their optimized band gap (typically <3.0 eV), which facilitate visible-light-driven redox reaction[6]. The catalytic activity in this spinel ferrite is further influenced by factor such as cation composition, synthesis conditions, and the presence of dopants, which can significantly alter their photocatalytic efficiency and stability[7,8]. This performance is intrinsically linked to parameter such as crystallite size, degree of crystallinity, and the accessibility of active surface sites, all of which directly dictate the generation of reactive radical crucial for effective dye degradation.

Ni^{2+} contributes to the magnetic behavior and structural stability of the spinel lattice, while Cu^{2+} can modify the cation distribution, lattice parameters, magnetic interactions, and surface reactivity because of its specific site preference and electronic configuration. Zn^{2+} is a non-magnetic ion with a strong preference for tetrahedral sites and can influence the distribution of Fe^{3+} ions between tetrahedral and octahedral sites, thereby modifying the superexchange interactions and magnetic properties. The incorporation of these three divalent cations in the selected ratio therefore provides a means of tuning the structural, magnetic, and surface properties of the ferrite. Furthermore, precise doping allows for the modulation of electronic band structures and charge carrier dynamics, thereby optimizing light absorption and reducing recombination rates to maximize photocatalytic output[9]. Nickel-doped cobalt ferrite nanoparticles, have demonstrated high catalytic efficiency in reducing nitroaromatic compounds and photo-oxidatively degrading toxic dyes[10,]. The inherent magnetic properties of spinel ferrite also enable their facile recovery and reuse, an important consideration for practical wastewater treatment applications[11]. The impressive photocatalytic activity of modified and engineered spinel ferrite, attributed to their favorable band gap energies, allows for efficient absorption of UV or visible light, thereby initiating photocatalytic reactions[9]. Moreover, the incorporation of

.

advanced materials into binary and ternary spinel ferrite nanocomposites has been shown to enhance light utilization, reduce electron-hole recombination, and mitigate agglomeration, leading to superior photocatalytic performance[12]. Specifically, the narrow band gaps of spinel ferrite allow for a broader absorption spectrum, including visible light, which constitutes a significant portion of the solar spectrum, thereby increasing their photocatalytic efficiency[13,14].

The nanoferrite with the composition $Ni_{0.4}Cu_{0.2}Zn_{0.4}Fe_2O_4$ are of particular research interest as they optimize the magnetic contributions of Ni, sintering facilitation of Cu, and saturation magnetization of Zn[15]. This synergistic composition enhances their efficacy in photocatalytic applications for environmental remediation. Recent research has shifted toward the nanoscale synthesis of these materials to exploit size-dependent phenomena. Furthermore, the semiconducting nature of ferrite, coupled with their magnetic recoverability, has opened new avenues in photocatalysis, particularly for the degradation of organic pollutants in wastewater[16,17].

The sol-gel auto-combustion technique is widely preferred for synthesizing high-quality spinel ferrite due to its exceptional ability to ensure precise stoichiometric control, facilitate homogeneous precursor distribution, and produce nanostructured powders with superior purity[18,19]. This process relies on a self-propagating exothermic reaction between metal nitrates and organic fuels such as citric acid or diethanolamine, which ensures the efficient formation of a viscous gel that decomposes into fine, phase-pure ferrite particles[21,22]. Compared to traditional ceramic processing, which often requires high-temperature calcination and prolonged sintering to achieve the desired phase, sol-gel auto-combustion significantly lowers the energy barrier for spinel phase formation[23]. $Ni_{0.4}Cu_{0.2}Zn_{0.4}Fe_2O_4$ nanoparticles were successfully synthesized by Awati et al. via this route, achieving high crystallinity through controlled calcination at temperatures of 400–700 °C[21]. While alternative methods such as aqueous co-precipitation is often augmented by ultrasonic irradiation to promote nucleation and restrict particle size are viable[24,25], sol-gel combustion remains uniquely advantageous for achieving the high structural homogeneity required for efficient photocatalytic performance. Furthermore, specialized processing like Rapid Thermal Annealing is generally reserved for distinct applications such as thin-film fabrication, where precise, rapid control over grain size and phase development is paramount[26].

2. Materials and Methods

.

All reagents were procured from Sigma-Aldrich and used without further purification to maintain experimental consistency. Analytical reagent (AR) grade copper nitrate trihydrate [$Cu(NO_3)_2 \cdot 3H_2O$], zinc nitrate hexahydrate [$Zn(NO_3)_2 \cdot 6H_2O$], nickel nitrate hexahydrate [$Ni(NO_3)_2 \cdot 6H_2O$], and iron nitrate nonahydrate [$Fe(NO_3)_3 \cdot 9H_2O$] were used as precursor salts without further purification. Citric acid was utilized as a chelating agent. The liquor ammonia used to adjuste to pH adjustment. Milli-Q water was used throughout the synthesis process.

2.1 Synthesis Procedure

$Ni_{0.4}Cu_{0.2}Zn_{0.4}Fe_2O_4$ nanoferrite were synthesized via a self-propagating auto-combustion method, a robust technique ensuring precise stoichiometric control and homogeneous mixing of precursor, effectively yielding fine, high-quality ferrite powder.[19] Stoichiometric amounts of 1.163 g $Ni(NO_3)_2 \cdot 6H_2O$, 0.483 g $Cu(NO_3)_2 \cdot 3H_2O$, 1.190 g $Zn(NO_3)_2 \cdot 6H_2O$, and 8.080 g $Fe(NO_3)_3 \cdot 9H_2O$ were dissolved in Milli-Q water and mixed to obtain a total precursor volume of 100 mL and stirred at 70 °C for 15 min to obtain clear and homogeneous solution. These solutions were then combined to form a single precursor mixture and further stirred at 100°C for 40 min to ensure the uniform distribution of metal ions. An aqueous citric acid solution 5.76 g ($C_6H_8O_7$) was subsequently added to the mixed nitrate solution under continuous stirring to promote chelation and complex formation. The pH of the solution was carefully adjusted to approximately neutral (pH ≈ 7) by the slow dropwise addition of liquor ammonia, a critical step to enhance metal cation binding to citrate ions and facilitate the formation of stable complex precursor, thereby preventing the premature precipitation of metal hydroxide .The resulting homogeneous solution was maintained at 100°C under continuous stirring until gradual solvent evaporation led to the formation of a viscous gel.[20] Upon further heating, the gel underwent spontaneous foaming followed by auto-ignition, initiating a rapid self-sustaining combustion reaction. The auto-combustion process concluded rapidly, yielding a fine, fluffy brown precursor powder. The as-combusted powders were subsequently subjected to calcination at 200^0C for 2 hours. This thermal processing is essential to eliminate residual organic species, facilitate the removal of intermediate phase, and promote the maturation of a well-ordered spinel lattice. Precise control over these thermal parameters effectively enhances the crystallinity and phase purity of the $Ni_{0.4}Cu_{0.2}Zn_{0.4}Fe_2O_4$ nanoferrite, thereby ensuring optimal structural and magnetic performance[27].

.

3. Results and Discussions

3.1 Characterization of $Ni_{0.4}Cu_{0.2}Zn_{0.4}Fe_2O_4$

A comprehensive structural characterization of the synthesized $Ni_{0.4}Cu_{0.2}Zn_{0.4}Fe_2O_4$ nanoferrite was carried out using X-ray diffraction (XRD), Fourier transform infrared (FTIR) spectroscopy, scanning electron microscopy (SEM), high-resolution transmission electron microscopy (HRTEM), and energy-dispersive X-ray spectroscopy (EDS). These complementary techniques were employed to investigate the crystal structure, phase purity, lattice vibrations, local cation distribution, morphology, particle size, crystallinity, and elemental composition of the synthesized nanoferrite. The combined analyses provide a comprehensive understanding of the structural characteristics of the material and establish the correlation between its microstructure and the observed magnetic and photocatalytic properties.

3.2. X-ray Diffraction Study

The X-ray diffraction was carried out using Philips x-ray diffractometer with the help of *CuKα* radiations (λ=1.5405Å). X-ray diffraction (XRD) patterns (Fig, 1) of $Ni_{0.4}Cu_{0.2}Zn_{0.4}Fe_2O_4$ show characteristic peaks corresponding to the (220), (311), (400), (422), (511), and (440) planes of the cubic spinel structure[21]. Studies indicate that the materials are generally single-phase, although higher calcination temperatures are often required to achieve full crystallinity[24]. A typical fingerprint peak of spinel ferrite, the prominent (311) reflection, verifies the production of a well-crystallized spinel phase.[25] The XRD pattern (Fig, 1) confirms the successful formation of a well-crystallized, single-phase cubic spinel structure, exhibiting reflections consistent with the standard JCPDS card No. 39-1277. The absence of secondary impurity peaks across the diffraction profile provides robust evidence of high phase purity, verifying the structural integrity of the synthesized . $Ni_{0.4}Cu_{0.2}Zn_{0.4}Fe_2O_4$ nanoferrite within the detection limits of XRD [32].

.

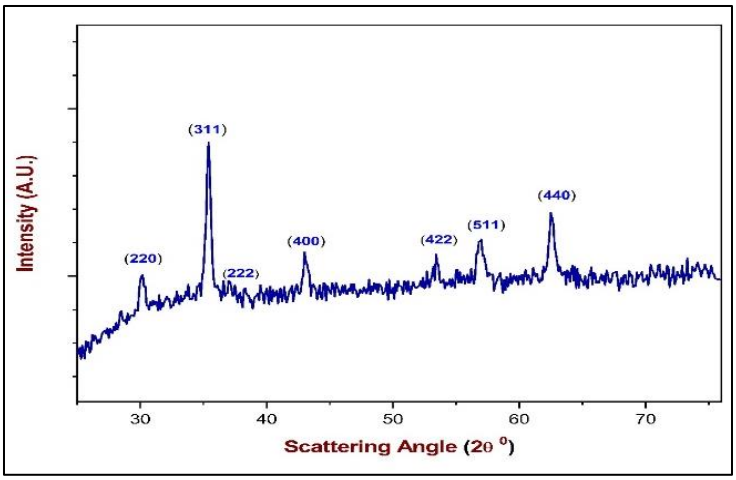


Fig. 1: XRD pattern of $Ni_{0.4}Cu_{0.2}Zn_{0.4}Fe_2O_4$

The moderate peak broadening suggests nanoscale crystallite size and possible lattice strain effects, which are commonly observed in nanocrystalline ferrite synthesized via chemical routes[31]. The observed diffraction pattern therefore confirms the successful synthesis of $Ni_{0.4}Cu_{0.2}Zn_{0.4}Fe_2O_4$ with cubic Fd-3m symmetry.

The lattice parameter is an important structural parameter that describes the dimensions of the unit cell. For a cubic crystal system, the interplanar spacing (d) and lattice parameter (a) are related through the Miller indices according to the following equation:

$$\boldsymbol{a = d\sqrt{(h^2 + k^2 + l^2)}} \qquad \textbf{(1)}$$

where a is the lattice parameter, d is the interplanar spacing, and h, k, and l are the Miller indices of the corresponding diffraction plane. The interplanar spacing can be determined using Bragg's law:

$$\boldsymbol{n\,x\,\lambda = 2d\,x\,sin\,\theta} \qquad \textbf{(2)}$$

where n is the diffraction order, λ is the wavelength of the X-rays incident on the crystal and θ is the Bragg diffraction angle. The calculated lattice parameter of the $Ni_{0.4}Cu_{0.2}Zn_{0.4}Fe_2O_4$ nanoferrite was found to be 8.3633 Å. This value is that of the unit-cell dimension of the material prepared and is compatible with the structure analysis of the cubic ferrite system. The lattice parameter can be used as a guide in determining the crystal structure and comparing the material to those of reported spinel ferrite. This is a characteristic value for the spinel phase and can differ slightly, depending on the synthesis conditions and composition, ranging from 8.370-8.389 Å in substituted systems[15], to 8.42867 Å in related ferrite structures[37]. X-ray diffraction analysis is

.

considered as a basic tool for confirming the formation of the cubic spinel phase and determination of the accurate lattice parameters and calculation of average crystallite size which together give the structural integrity of the synthesized nanoferrite [25,27].

The characteristic XRD diffraction peak broadening was used to calculate the average crystallite size according to the Debye-Scherrer equation:

$$D = K x \lambda / (\beta cos \theta) \qquad (3)$$

where D is the average crystallite size, K is the shape factor (typically around 0.9), λ is the wavelength of the X-rays, β is the full width at half-maximum (FWHM) of the diffraction peak, and is the Bragg angle. The average crystallite size was determined using measured diffraction peak parameters, and found to be 15.17 nm. This crystallite size is very small, suggesting that the prepared ferrite has a fine crystalline structure. The calculated size of the coherent diffraction domain should not be taken as the particle or grain size directly, as it is an approximation based on the Scherrer equation.

Extensive literature shows that wet chemical synthesis routes can produce Ni-Cu-Zn ferrite with a precise control of nanometre size dimensions of crystallites. The crystallite sizes of the samples prepared by the ultrasonic irradiation method are less than 40 nm [25], and those prepared by the microwave and conventional sintering methods are in the range of 33–39 nm [34]. Moreover, the crystallite size can be reduced to as small as 17.75–20.15 nm,[28] and crystallite morphology analyses by SEM for similar compositions are often found to be in the range of 69–88 nm.[35] The results confirm the effectiveness of wet chemical approach in controlling the grain growth to nanoscale. Other sol-gel studies, however, have indicated that much smaller grain sizes are obtained, for instance the films calcined at 600°C have an average grain size of ~ 20 nm[36.] The variation underscores the importance of the role of calcination temperature and precursor chemistry on the initiation and development of the grains and should be taken in the context of the synthesis route used in this report.

The theoretical X-ray density (D_x) was calculated using the crystallographic unit-cell parameters and the molar mass of the ferrite according to the following equation:

$$D_x = Z x M / (N_a a^3) \qquad (4)$$

Z is the number of formula units per unit cell, M is the molar mass of $Ni_{0.4}Cu_{0.2}Zn_{0.4}Fe_2O_4$, N_a is Avogadro's constant and a is the lattice parameter in centimetres. The unit cell of a cubic spinel is a spinel (Z = 8). The X-ray density calculated was 2.9569 g cm^{-3}. It is a theoretical parameter

.

that is helpful when comparing with the experimentally determined bulk density and is helpful for estimating the porosity of the prepared sample. In addition, the bulk density (D_β) was calculated using the mass of the pelletized samples and their geometric volume, which also gives an indication of the packing. The reported values depend on the composition, form of the sample, and its preparation method: For $Ni_{0.5}Zn_{0.5}Fe_2O_4$ nanoparticles, the value was reported to be 1.46 g/cm³; and for bulk Ni–Zn ferrite, the value was reported to be 4.68–5.80 g/cm³ [53,54]. The significance of the influence of porosity and the measurement method on the density values for porous Ni–Zn ferrite powders is also indicated by the reported values of the density of 0.76–0.78 $g.cm^{-3}$, as compared to the conventional Ni–Zn ferrite that has a density of ~2.3 $g.cm^{-3}$

The unit-cell parameters and the molar mass of the ferrite were used to calculate the theoretical X-ray density (D_x) using the following equation::

$$\boldsymbol{D_\beta = m / V} \qquad \textbf{(5)}$$

An important physical parameter that describes the fraction of the bulk volume related to voids is called as porosity. The X-ray density and bulk density values were used to determine the estimated fractional porosity (P):

$$\boldsymbol{P = 1 - (D_\beta / D_x)} \qquad \textbf{(6)}$$

The porosity percentage was obtained using:

$$\boldsymbol{P\,(\%) = [1 - (D_\beta / D_x)] \times 100} \qquad \textbf{(7)}$$

The value of the porosity was 0.3142 or 31.42% from the reported values of density. This value is a difference between the theoretical crystallographic density and bulk density. This difference may be due to the interparticle void, pores and packing effect in the prepared material. Compared to this, ceramic processed Ni–Zn ferrite with Al content have been reported with bulk densities of 4.79–4.96 g cm^{-3} and X-ray densities of 5.31–5.37 g cm^{-3}, which shows how the density of the ferrite can be influenced by both composition and densification.

In general, the XRD derived parameters give information about the unit-cell dimensions and nanoscale crystalline domains of the prepared nanoferrite $Ni_{0.4}Cu_{0.2}Zn_{0.4}Fe_2O_4$..

3.3 FTIR Study

The Fourier Transform Infrared (FTIR) spectrum (Fig. 2) confirmed the formation of the cubic spinel ferrite structure and the identification of intrinsic metal–oxygen bonding vibrations in

.

$Ni_{0.4}Cu_{0.2}Zn_{0.4}Fe_2O_4$. The recorded FTIR spectrum of the sample shows two bands of characteristic absorption in the low wavenumber region in the range 400-4000 cm-[1] [25,] The features are intrinsic metal–oxygen stretching vibrations at tetrahedral and octahedral sites, which clearly indicates the successful synthesis of a single-phase spinel ferrite[27].

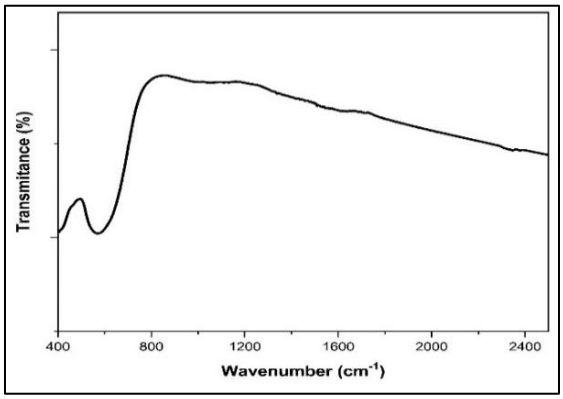


Fig. 2: FTIR Spectrum of $Ni_{0.4}Cu_{0.2}Zn_{0.4}Fe_2O_4$

Specifically, the high frequency band around 580 cm^{-1} is assigned to the stretching of metal–Oxygen bonds at tetrahedral (Td) sites, while the low frequency band around 400 to 450 cm^{-1} is assigned to the stretching of metal– Oxygen bonds at octahedral (Oh) sites[27]. The band positions and their frequency difference is also related to the cation distribution in the lattice, with Zn^{2+} being coordinated in tetrahedral sites and Ni^{2+} and Cu^{2+} being coordinated in octahedral sites[27].

In terms of the extrinsic features, a weak and broad band at ∼1600 cm^{-1} corresponds to the bending vibration of surface-adsorbed water molecules[24], while a broad band at ∼2300-2400 cm^{-1} is due to the adsorption of atmospheric CO_2 during measurement. These are typical features of wet-chemically made ferrite, and are not the presence of impurity phases [27]. The absence of any other absorption bands corresponding to the secondary iron oxides or the metal oxides further supports the high phase purity of the synthesized ferrite [31.]

3.4 SEM Study

The SEM–EDS elemental mapping (Fig. 3 a) reveals the distribution of nickel (Ni), copper (Cu), and zinc (Zn) throughout the sample Field-emission scanning electron microscopy (FE-SEM) (Fig. 3 b) micrographs reveal granular, nearly spherical to irregular nanograins clustered into agglomerates with non-uniform surface texture[31]. This agglomeration is attributed to intrinsic magnetic dipole–dipole interactions and high surface energy effects characteristic of

.

nanostructured spinel ferrite[19,21] The absence of secondary morphologies or abnormal grain growth confirms the high phase purity, structural homogeneity, and compositional verification of the synthesized ferrite [31]. These particle size distributions and agglomeration characteristics play a critical role in dictating the material's magnetic and catalytic performance [32].

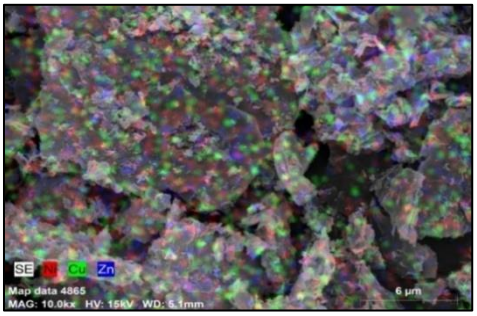


Fig. 3 a : SEM–EDS elemental mapping of the sample showing the spatial distribution of nickel (Ni), copper (Cu), and zinc (Zn).

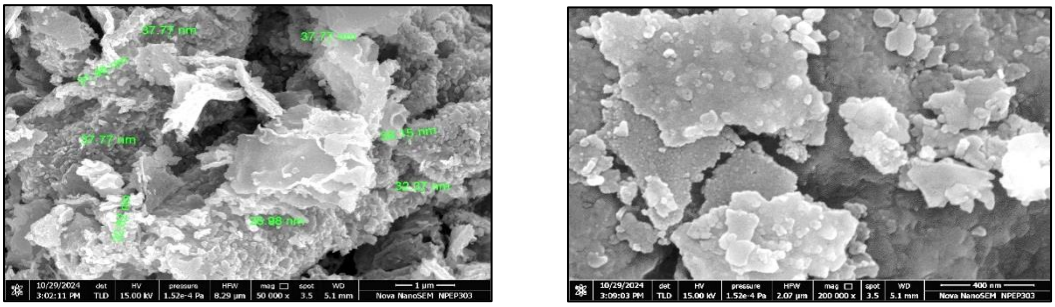


Fig. 3 b : SEM Images of $Ni_{0.4}Cu_{0.2}Zn_{0.4}Fe_2O_4$

At higher magnifications (Fi**g.** 3 b), quantitative particle size distribution analysis yields a narrow, near-Gaussian distribution (Fig. 4**)** with a mean particle diameter of 43.53 nm and a standard This size range is typical for high-quality spinel ferrite produced via wet-chemical or sol–gel routes, demonstrating precise synthesis control and uniform nucleation and growth kinetics [27]. Such structural and morphological uniformity ensures reproducible magnetic and catalytic activity for advanced applications [34].

.

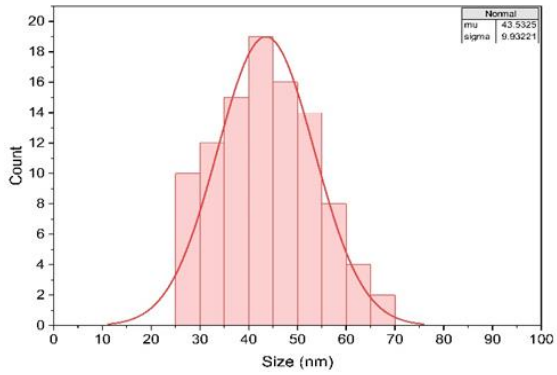


Fig. 4: SEM - Gaussian curve of particle size $Ni_{0.4}Cu_{0.2}Zn_{0.4}Fe_2O_4$

3.5 Elemental Mapping (EDS Analysis)

The synthesized sample $Ni_{0.4}Cu_{0.2}Zn_{0.4}Fe_2O_4$ was confirmed by energy-dispersive X-ray spectroscopy (EDS) analysis, which showed no impurities in the sample[15]. The homogeneity of distribution of these constituent elements in the analyzed regions was also confirmed by complementary elemental mapping, which revealed a high uniformity in the distribution of elements in the analyzed areas;[31]. Moreover, this uniform elemental distribution throughout the sample confirms the sample has a spinel structure and that no phase segregation has occurred[38]. Such elemental uniformity is ideal for maintaining uniform physical and chemical properties throughout the material, especially if the material is used as a catalyst that is required to have uniform active sites .

.

.

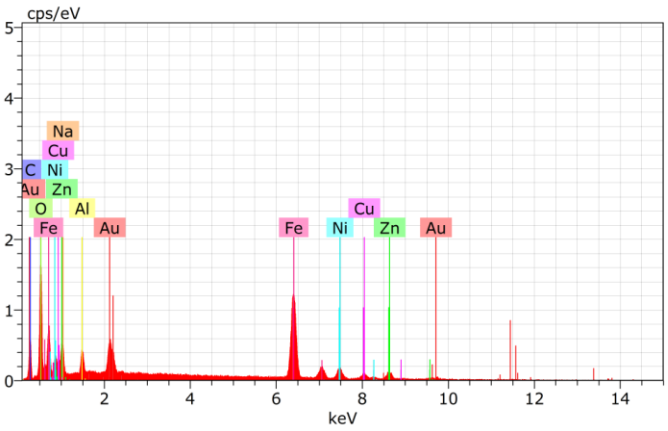


Fig. 5: EDS spectra of $Ni_{0.4}Cu_{0.2}Zn_{0.4}Fe_2O_4$

The energy dispersive X-ray spectroscopy (EDS) mapping (Fig. 5) verifies the elemental compositions, showing that Ni, Cu, Zn, Fe and O are present in the synthesized ferrite matrix [15]. Maps of the elemental distribution reveal a homogeneous spatial distribution of all these constituent elements, typical of a very homogeneous chemical composition, and the successful incorporation of all metallic species in the spinel lattice[27]. The Au signal is probably due to a conductive coating that was applied to the sample before SEM–EDS analysis. The Al signal may arise from the aluminium sample mounting accessories used during the analysis and the Na signal may come from minor surface contamination during sampling mounting or handling materials. These are, therefore, extrinsic signals and not dopants or constituents of the synthesized ferrite. Furthermore, no interference peak due to elemental signals is observed, indicating that the phase purity and accuracy of the [24] stoichiometric compositions obtained is crucial for the preparation of a structurally stable synthesized ferrite. Elemental distribution maps show the uniform distribution of these constituent elements within each of the areas investigated, indicating the very homogeneous chemical composition of these areas, and the successful incorporation of each of the metallic species into the spinel lattice [27]. Most importantly, elemental segregation or clustering of elements will be verified if it is absent, which is a desired compositional uniformity across the material. Furthermore, the lack of other elemental signals is not only an indication of the high phase purity of the obtained sample, but also provides evidence of the correct stoichiometric control necessary for maintaining the functional and structural performance [27]. Thermodynamically, tetrahedral sites (A) are preferred for the occupation by Zn^{2+} ions and octahedral sites (B) are the preferred sites for Ni^{2+} and Cu^{2+} ions, as seen with the

.

Ni–Cu–Zn ferrite[27,29]. The selective substitution of non-magnetic Zn^{2+} at A-sites has a significant effect on the magnetic superexchange interactions between A and B sublattices, modulating the magnetic parameters and optimizing the availability of catalytically active sites. The uniformity observed in the elemental mapping also indicates good incorporation into the spinel lattice, in line with the high phase purity as well as high structural homogeneity confirmed by X-ray diffraction (XRD) analysis.

3.6 HR-TEM

The HR-TEM micrograph (Fig. 6 (a)) reveals the presence of nearly spherical to irregularly shaped nanoparticles and the noticeable agglomeration. The dense packing of these particles is likely due to magnetic dipole–dipole interactions and high surface energy, which are typical of spinel ferrite nanostructures.[25]. Furthermore, the contrast variation in the micrograph indicates the existence of nanocrystalline domains in aggregated clusters. The estimated particle sizes from TEM analysis falls within the range of 12.8–35.2 nm with an average size of 23.9 nm, a median size of 23.5 nm and right-skewness due to minor agglomeration and minor particle size distribution corresponding to bigger particle sizes.

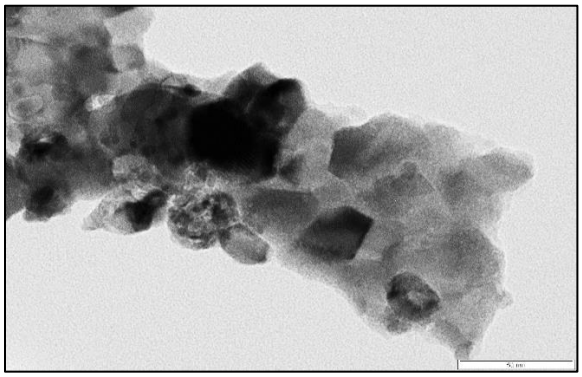


Fig. 6 (a) HR-TEM

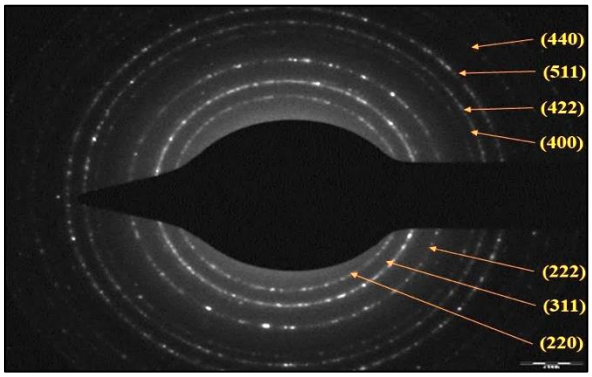


Fig. 6 (b) SAED Pattern image of $Ni_{0.4}Cu_{0.2}Zn_{0.4}Fe_2O_4$

.

The SAED pattern (Fig. 6(b)) contains a set of concentric diffraction rings formed by the bright spots, characteristic of the polycrystalline nature of the sample. The nanoparticles are domains of randomly oriented nanocrystals, not single-crystalline domains[21], as suggested by the ring pattern. The diffraction rings can be identified as the characteristic planes of the cubic spinel ferrite structure; most commonly (220), (311), (400), (422), (511), and (440) reflections as in.

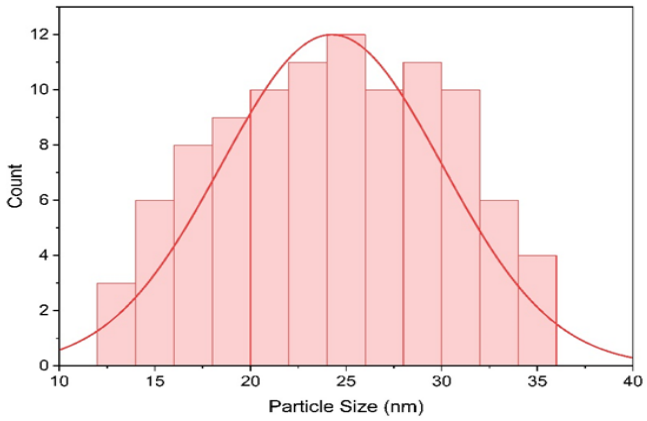


Fig. 7: HR-TEM Particle size distribution histogram of $Ni_{0.4}Cu_{0.2}Zn_{0.4}Fe_2O_4$

the standard JCPDS data for spinel ferrite[33]. From the appearance of sharp and well-defined rings, it is confirmed that the synthesized material has a high crystallinity.

The formation of high quality, polycrystalline spinel ferrite nanoparticles are confirmed using the TEM and SAED analyses. The presence of a unimodal particle size distribution, together with a diffraction pattern of sharp and well resolved diffraction rings, clearly indicates the high phase purity and structural homogeneity of the material [16, 21]. Structural uniformity is important for optimizing the material's performance in magnetic and catalytic applications and these well-controlled morphological and crystalline characteristics are essential for this[25].The particle size distribution histogram shows a distinct unimodal and nearly Gaussian distribution (Fig.7**)** indicating a homogeneous formation of the nanocrystalline ferrite phase. This symmetrical distribution indicates well controlled nucleation and growth process which results in high structural uniformity and low polydispersity effects with respect to the material's structural and surface properties.

The size of the particles is distributed mainly in the size range of 15 to 35 nm and the highest frequency is in the middle of this range of 24 to 26 nm, The fitted normal curve is symmetric,

.

highlighting the effectiveness of the synthesis protocol to keep the synthesis conditions at a more or less constant level, which results in a very narrow particle size distribution [16]. This is an important aspect of the limited polydispersity because it reduces variations in the surface and structural energies that might hinder uniform functional response, leading to the uniform magnetic and catalytic performance required for these spinel ferrite nanostructures[25.] In addition, the small size of the particles gives a high surface-to-volume ratio that improves surface-dependent phenomena, like adsorption and photocatalytic activity[21].The values of skewness and secondary peaks are negligible and suggest that there are no major secondary growth phases or aggregation induced size anomalies. Overall, the distribution indicates the successful synthesis of nanometer-size uniformly sized nanoferrite having well-controlled morphological characteristics, which is a prerequisite for obtaining reproducible optical properties and photocalytic properties [38].

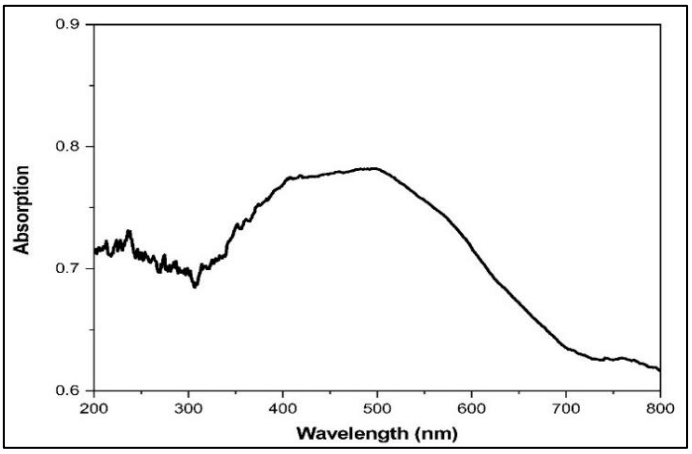
3.7 Optical Characterization

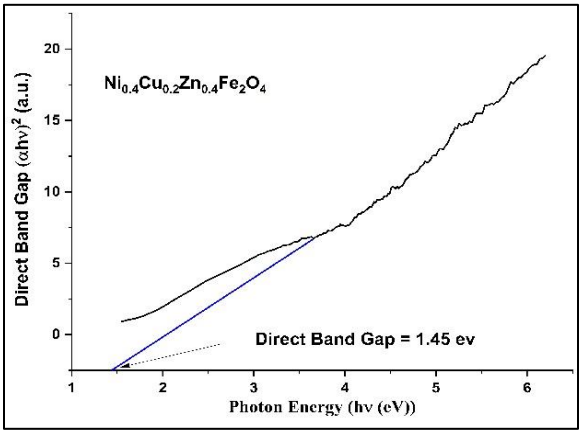
The UV–Visible absorption spectrum (Fig. 8 (a)**)** shows a broad absorbance profile starting from the ultraviolet and increasing gradually and reaching a peak around 480 to 500 nm falling gradually towards the near-infrared region. The metallic cations and oxygen anions ($O^{2-} \rightarrow Fe^{3+}$) exhibit the same charge transfer transition as is characteristic of spinel ferrite[29], and is the reason for the broad absorption band in the visible region. The shape of the curves does not show any typical excitonic peaks, which suggests the formation of nanocrystalline particles with size-induced band broadening effects[51]

To determine the optical band gap, UV-Visible spectroscopy is used to make a Tauc plot [30]. The analysis allows for accurate calculations of the direct (Fig. 8 (b)) and indirect band gap (Fig. 8 (b)) and thus provides an insightful electronic band structure of the material, which is relevant for advanced use in optoelectronic and photocatalytic applications[39]. The Tauc plot analysis of the $Ni_{0.4}Cu_{0.2}Zn_{0.4}Fe_2O_4$ sample confirms the semiconducting nature of the prepared material and also provides significant information about the electronic transitions in the sample which is necessary for efficient harvesting of visible light for solar energy. Zinc Ferrite nanoparticles with similar structures have been reported to exhibit an indirect band gap transition at about 650 nm, which is in good agreement with the density functional theory calculations[49]. The measured band gap value of 2.26 eV for the pure zinc ferrite nanoparticles, which then shows a sharp decrease with increasing nickel concentration, is consistent with other nickel substituted zinc ferrite

.

systems[50]. This sensitivity is also supported by compositional studies of NiCdAlFeO ferrite, which revealed a decrease in the band gap energies from 2.587 eV to 2.166 eV as the content of Ni increased[29], and related systems such as $NiFe_2O_4$, Mn-doped $NiFe_2O_4$ and Zn-doped $NiFe_2O_4$ with about 1.984 eV, 1.954 eV and 1.973 eV as Ni content increased [51]. These variations reflect the ability to control optical characteristics of the composition to precisely optimize the photocatalytic activity of the hybrid materials in the visible light region and the efficiency of charge transfer[37] This implies that the band gap can be tuned in the range of the characteristic band gap of these ferrites, making them an excellent material for light-harvesting and photocatalytic applications.[41]





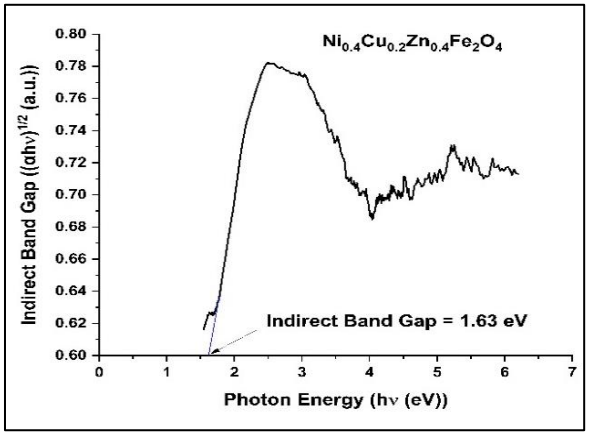


Fig. 8 (a): UV-DRS Spectra of $Ni_{0.4}Cu_{0.2}Zn_{0.4}Fe_2O_4$

Fig. 8 (b): Direct Band Gap: 1.45 eV **Fig. 8 (c):** Indirect Band Gap: 1.63 eV

The high absorption in the visible region implies better capability of harvesting photons, desirable for photocatalytic and optoelectronic applications. In addition, the longer absorption tail

.

to the higher wavelengths could be related to the defect states and localized energy level defects produced during synthesis, which could lead to an enhanced activity for visible light[30]. In general, these spectral characteristics with the high value of visible-light absorption and the tunable band gap further validate the synthesis of high-quality ferrite nanostructures. The structural integrity along with these attributes ensure electronic framework required for efficient charge transfer and makes these nanoparticles excellent light-harvesting and visible light driven photocatalytic degradation candidates of organic pollutants[40]. From UV-Visible absorption spectra, the optical band gap of NiCuZn ferrite nanoparticles was calculated using the Tauc relation[30,] which showed that the bands are direct and indirect band gap with value of 1.45 eV and 1.63 eV, respectively. The observed decrease in the optical band gap relative to the bulk ferrite is attributed mainly to a combination of size-dependent quantum confinement effects and of the redistribution of the cations between tetrahedral and octahedral sites, and the appearance of defect-induced localized states in the forbidden band region[25.] The band gap narrowing leads to better photocatalytic activity under visible light irradiations and charge transfer efficiency.[30] The narrow indirect band gap helps to lower the threshold energy required for an electric transition, which facilitates the formation of a photogenerated electron–hole pair under the visible-light irradiation, and promotes efficient charge-carrier separation, and suppresses charge-carrier recombination[31]. This is beneficial for the photocatalytic degradation of organic pollutants under visible-light irradiation and other optoelectronic applications.[48]

3.8 Magnetic Characterization

The magnetic property of $Ni_{0.4}Cu_{0.2}Zn_{0.4}Fe_2O_4$ can change depending on the synthesis conditions of grain size and the distribution of cations between the tetrahedral (A) and octahedral (B) positions. Many different values of saturation magnetization (Ms) are found in the literature. The $Ni_{0.4}Cu_{0.2}Zn_{0.4}Fe_2O_4$ powders prepared by the above-mentioned method had a value of 72.4 emu/g, while the same composition in the thin films, prepared by the sol-gel and RTA method at 600 °C, was found to have a value of ~ 300 emu/g (or ~ 228.877 emu/cm³ in related sol-gel film studies). The coercivity is very low, and these ferrites are termed as soft magnetic ferrite. Specifically, the value of 9.7 Oe has been reported.[33] This low coercivity is very desirable for use in materials that have a high magnetic permeability and low magnetic hysteresis loss like sensitive electronic components, inductor and transformer cores for energy efficiency applications. The presence of dopants also affects the magnetic properties. The average grain

.

size and the magnetic moments[23] are decreased by Ti substitution ($Ni_{0.4}Cu_{0.2}Zn_{0.4}Fe_2$-$xTi_xO_4$). The magnetic properties obtained from the magnetic hysteresis loop (Fig. 9) were saturation magnetization (Ms) = 34.76 emu g^{-1}, remanent magnetization (Mr) = 17.40 emu g^{-1} and coercivity (Hc) = 6.438 kOe, which gave important data about the magnetic ordering and domain properties.

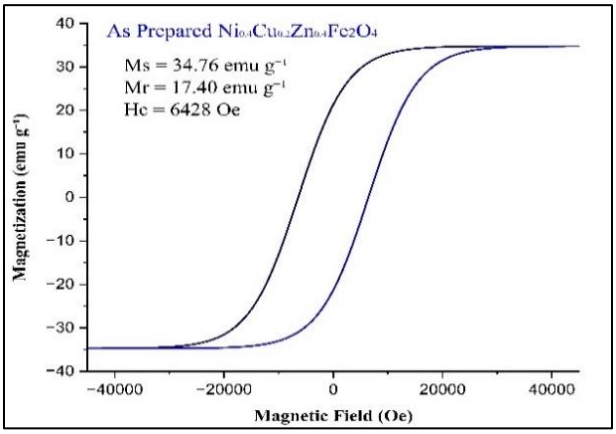


Fig. 9: VSM spectra of $Ni_{0.4}Cu_{0.2}Zn_{0.4}Fe_2O_4$

The saturation magnetization values observed are also remarkable, and this is normal for magnetic material with very small particle size, but the excellent shape of the ferrimagnetic hysteresis loop (no unwanted secondary magnetic phases) suggests a high magnetic homogeneity and no secondary magnetic phases that affect the material. This simple calculation of the Mr/Ms ratio further supports the presence of stable single domain or pseudo single domain particles that is indicative of the structural consistency of the synthesised $NiCuZnFe_2O_4$ photocatalyst with the sufficient saturation magnetization with which the particles can be easily separated from the reaction medium by the use of an external magnetic field. The material has a relatively high coercivity and the response to the magnetic field is adequate to ensure a rapid and efficient recovery.[55]

4.0 Photocatalytic degradation study of Congo Red (CR) dye

The extensive discharge of synthetic dyes from the textile, leather, paper, and printing industries has become a significant source of water pollution, creating serious environmental and health problems,[16] with one of the most commonly used dyes being the benzidine-based Congo Red

.

(CR) dye for cotton and paper. Due to its complicated molecular structure, high molecular weight, azo (–N=N–) linkages, Congo Red has very high chemical stability and natural resistance to degradation and is a difficult material to treat by traditional environmental remediation methods. In addition, CR is known to be carcinogenic, mutagenic and toxic, and is therefore a highly significant environmental problem related to the removal of it from wastewater.[43]

Nanostructured spinel ferrite (MFe_2O_4) has proven to be quite promising photocatalysts that are also magnetic, chemically stable and have low toxicity and absorb visible light. For photocatalytic applications, the optical band gap (Eg) is one of the important parameters. The data for the composition $Ni_{0.4}Cu_{0.2}Zn_{0.4}Fe_2O_4$ is limited in the sources provided but other Ni ferrite that are close to the composition are Ni-Cu-Zn ferrite and substituted Ni ferrite which have a range of band gap of 1.1–3.5 eV [30]. The band gaps of the Ni-Zn ferrite doped with Cu were found to vary from 2.80 to 3.50 eV[27,] . The composition of $NiFe_2O_4$ can be precisely controlled to obtain specific optical responses, e.g., $Ni_{0.4}Cu_{0.2}Zn_{0.4}Fe_2O_4$. Moreover, the band gap range of 1.1 - 3.5 eV [33,] is very suitable for visible-light photocatalysis. High removal efficiencies have been exhibited by the related Ni-Cu-Zn ferrite. Under visible light[77], the ZnO/$NiFe_2O4$ nanocomposite was able to degrade 92% of MB in 40 minutes. Nickel substituted Zn ferrite are also found to be better than zinc ferrite[22]. The degradation process is frequently pseudo-first order. One such example is $NiFe_2O_4$ nanoparticles, which have shown photocatalytic efficiency of 89% in the degradation of Methylene Blue and 92% in Methyl Orange dye in just 1 minute using the UV-C/H_2O_2 system, with reaction rate constants between 2.065 and 2.417 min^{-1} [57.] From an application point of view, magnetic recoverability is considered to be a key benefit of such ferrite catalysts. The $NiFe_2O_4$ photocatalysts are known to exhibit high stability, with a photocatalyst efficiency loss of just 6.0% after seven successive cycles [57]. Other research articles on Ni ferrite substituted with Nd also reported excellent recyclability and durability.[40] The photocatalytic degradation process of Congo Red dye by the efficient and reusable nanoferrite $Ni_{0.4}Cu_{0.2}Zn_{0.4}Fe_2O_4$ was explored in the presence of visible light. The present method is designed to provide sustainable and eco-friendly solution for dye contaminated wastewater treatment in compliance with green chemistry.[52]

.

4.1 Photocatalytic performance of $Ni_{0.4}Cu_{0.2}Zn_{0.4}Fe_2O_4$ nanoferrite

The UV-Vis absorption spectra of Congo Red solution in the presence of $Ni_{0.4}Cu_{0.2}Zn_{0.4}Fe_2O_4$ catalyst under natural sunlight showed a gradual decrease in the characteristic absorption peak at ~497 nm [44] with increasing irradiation time (Fig. 10a) The absorbance decreased to nearly zero after 350 min, indicating substantial degradation of the dye. The continuous reduction of the azo dye absorption band confirms the photocatalytic destruction of the chromophoric structure responsible for the color of Congo Red.[44] The absence of significant peak shifts suggests that the degradation proceeded mainly through the breakdown of dye molecules rather than the formation of stable-colored intermediates.

.

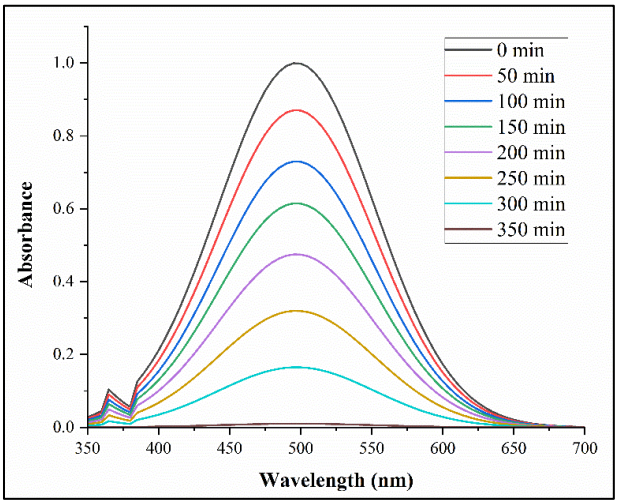


Fig.10 (a) : UV–Vis absorption spectra of 20 ppm Congo Red dye recorded at different irradiation time in the presence of $Ni_{0.4}Cu_{0.2}Zn_{0.4}Fe_2O_4$ (1 $g.L^{-1}$) spinel ferrite catalyst under natural sunlight condition.

The photocatalytic degradation profile was investigated, as shown Fig.10 (b) of Congo Red dye percentage photocatalytic degradation vs time under natural sunlight shows a progressive increase in degradation percentage with increasing irradiation time. The degradation increases almost linearly and reaches approximately 97–98% after 350 min of irradiation. This behavior indicates the gradual removal of Congo Red from the solution in the presence of the $Ni_{0.4}Cu_{0.2}Zn_{0.4}Fe_2O_4$ spinel ferrite catalyst. The observed photocatalytic activity suggests that the synthesized ferrite is a promising material for dye degradation under natural sunlight.[42]

.

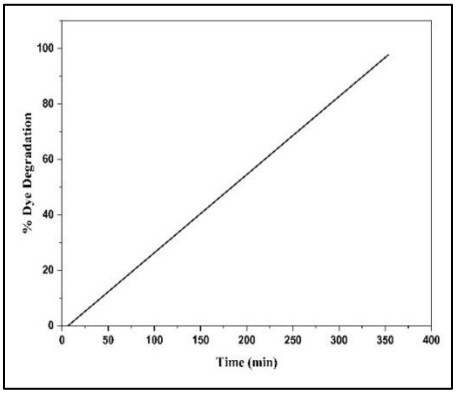


Fig.10 (b) : Time-dependent photocatalytic degradation of Congo Red dye under sunlight irradiation, expressed as percentage dye degradation versus irradiation time (min).

Under sunlight conditions, the photocatalytic degradation behavior of Congo Red dye was investigated, as shown in the A/A_0 versus time curve Figure 10 (c). The apparent degradation rate constant was found to be 0.0103 min^{-1}.[57] The linear fitting of $\ln(A_0/A)$ versus irradiation time yielded an R^2 value of 0.6966, indicating a moderate correlation with the pseudo-first-order model. The photocatalytic degradation activity under sunlight is mainly due to the efficient generation of electron – hole pairs in the $Ni_{0.4}Cu_{0.2}Zn_{0.4}Fe_2O_4$ catalyst after the absorption of visible-light photons [42].

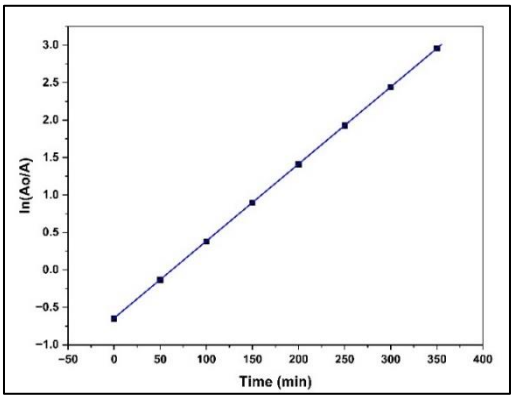


Fig.10 (c) Pseudo-first-order kinetic plot of ($\ln(A_0/At)$) versus irradiation time (min) for the photocatalytic degradation of the dye.

.

4.2 Effect of pH on the Degradation Time of Congo Red Dye

The effect of pH on the photocatalytic degradation process was systematically studied in the pH range of 2–12.[53.] The results of the experiments (Fig. 11) showed that the pH of the reaction medium is a crucial parameter that can influence the degradation efficiency by influencing the interfacial interactions between the spinel ferrite catalyst

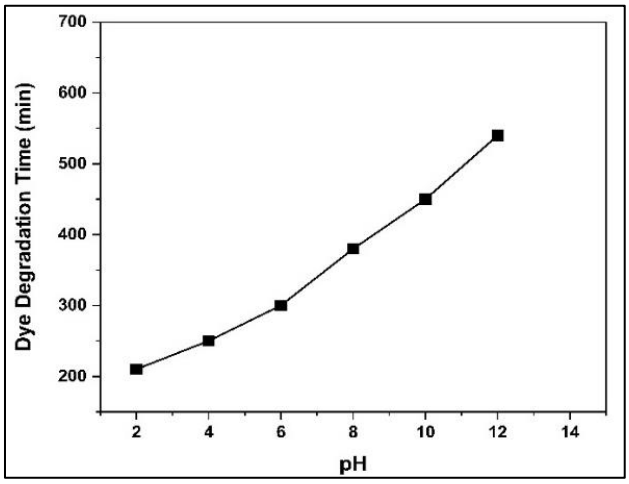


Fig. 11: Effect of pH on degradation time for 20 ppm Congo Red dye using $Ni_{0.4}Cu_{0.2}Zn_{0.4}Fe_2O_4$ (1 g L^{-1}) spinel ferrite catalyst under natural sunlight conditions.

and Congo Red dye. The degradation time increases slowly with increasing pH (above 6), but increases rapidly in acidic conditions pH 2–4,. The trend is controlled by the surface charge of the catalyst, and the ionization state of the dye. In acidic conditions the catalyst surface undergoes a positive charge making the anionic Congo Red molecules attracted strongly to the surface, thus leading to the adsorption and degradation of the molecules. On the other hand, under alkaline conditions electrostatic repulsion between the catalyst and the dye prevents the interaction and decreases the efficiency of degradation [53, 17.]

4.3 Scavenger Study

In the scavenger study (Fig. 12) , when isopropyl alcohol was added, the degradation of Congo

.

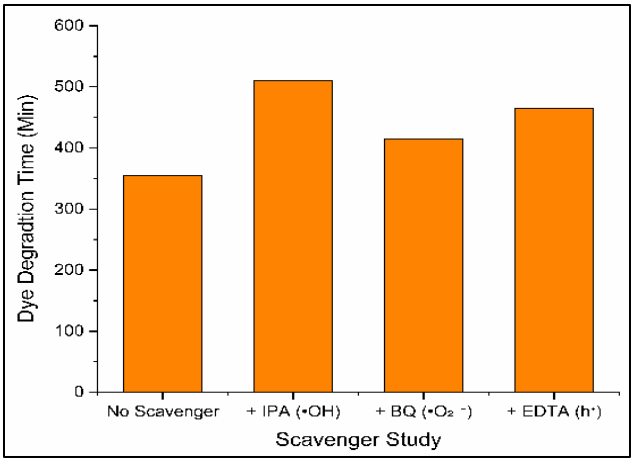


Fig. 12: Scavenger inhibition analysis of Congo Red dye in the presence of $Ni_{0.4}Cu_{0.2}Zn_{0.4}Fe_2O_4$ spinel ferrite catalyst.

Red was greatly reduced, strongly supporting the hypothesis that the most significant species [16] which are reacting is the hydroxyl radical (·OH). To unravel the mechanism of the photocatalytic degradation, radical scavenging experiments were conducted by using isopropanol (IPA), benzoquinone (BQ) and EDTA (ethylenediaminetetraacetic acid) as the radical scavengers for the hydroxyl radicals (•OH), the superoxide radicals ($•O_2^-$) and the photogenerated holes (h^+(VB)) respectively.[53] The marked loss of degradation efficiency when the selected scavengers (Fig. 12) were added provides a convincing proof that the degradation pathway is mainly initiated via hydroxyl radicals (•OH), superoxide radicals ($•O_2^-$) and photogenerated holes (h^+(VB)) which play a crucial role in the mineralization mechanism. These species are produced by the interaction of the photogenerated charge carriers, the dissolved oxygen and the water molecules.[42,46]

4.4 Reusability Study – Degradation Time of Congo Red Dye

The recyclability of the catalyst was evaluated through successive degradation cycles. The catalyst exhibited excellent structural stability and reusability over five consecutive cycles, with only a slight increase in degradation time observed.[11,16]

.

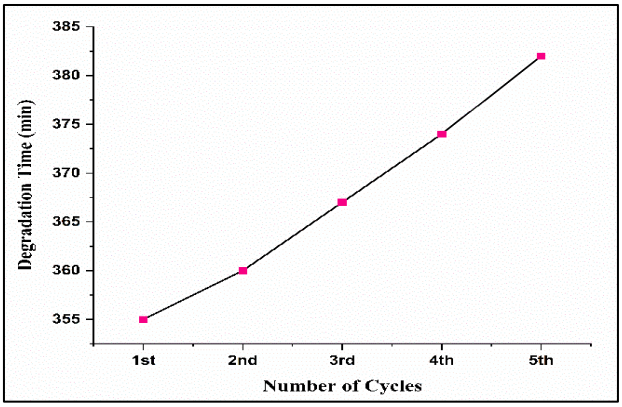


Fig.13. Reusability study of 20 ppm Congo Red dye in the presence of $Ni_{0.4}Cu_{0.2}Zn_{0.4}Fe_2O_4$ (1 g L^{-1}) spinel ferrite catalyst.

Each cycle of photocatalytic degradation was followed by separation of the catalyst from the reaction mixture using first of all a centrifugation method.[57] After the catalyst was recovered, it was then subjected to magnetic separation with an external permanent magnet to ensure the removal of any magnetic nanoferrite particles, and reduce catalyst loss during recovery. The separated catalyst was washed 2-3 times with Milli-Q water to wash away the adsorbed reaction products and dye molecules. The washed catalyst was dried in a hot-air oven at 80 °C until constant weight was reached, cooled at room temperature and then utilized in the next degradation run.[11] The recovered catalyst was used to a new dye solution at the same conditions for each recycling experiment. The same centrifugation, magnetic recovery, washing, drying and reusing process were performed after each degradation cycle. The $Ni_{0.4}Cu_{0.2}Zn_{0.4}Fe_2O_4$ nanoferrite displayed both good separation and recovery of fine particles of the catalyst and reusability, to make it useful as a recoverable photocatalyst.[16]

Magnetic nature of the catalyst enables easy separation and recovery from the reaction medium. More importantly, it is stable in the catalytic activity after five reuses, which shows high potential as a cost-effective sustainable material for wastewater treatment and other environmental applications.

.

Conclusions

The synthesis of $Ni_{0.4}Cu_{0.2}Zn_{0.4}Fe_2O_4$ nanoferrite via citric acid-assisted sol–gel method was accomplished, and the obtained product was shown to be efficient photocatalyst for degradation of Congo red dye in natural sunlight. The nanosized cubic spinel ferrite with an adequate optical and magnetic property was obtained by the XRD, SEM, HRTEM, FTIR, EDS, UV–Vis, and VSM analyses. The photocatalytic activity varied considerably with pH, and under acidic conditions, it was higher because of the favorable interaction of the surface charge and anionic Congo red. Scavenger studies revealed the participation of •OH, $\bullet O_2^-$ and h^+(VB) species in the photocatalytic degradation mechanism. The results indicated that $Ni_{0.4}Cu_{0.2}Zn_{0.4}Fe_2O_4$ was a potential reusable photocatalyst for treating dye-contaminated wastewater for sustainable applications.

Acknowledgement:
Authors would like to acknowledge DST for the accessibility of instruments procured under DST-FIST program at Chandmal Tarachand Bora College, Shirur File No: SR/FST/COLLEGE/068/2017.

Authors' Contributions:

Kiran Badave: Conceptualization, methodology, preparation of $Ni_{0.4}Cu_{0.2}Zn_{0.4}Fe_2O_4$ nanoferrite, photocatalytic experiments, data collection, analysis and interpretation of results, preparation of figures and tables, and writing of the original manuscript.

Shankar Thopate: Supervision, conceptual guidance, interpretation, and discussion of the results, critical review and revision of the manuscript and overall guidance of the research work.

Both authors participated in the final review of the paper and gave their approval for publication.

Conflict of Interest: The authors declare that they have no conflict of interest.

References

1. J. S. Shameran , M. M. Wali, 'Review on Magnetic Spinel Ferrite (MFe_2O_4) Nanoparticles: From Synthesis to Application'. *Heliyon*, 9, e16601, 2023.
2. M. A. Almessiere, Y. Slimani, A. D. Korkmaz, A. Baykal, H. Güngüneş, Sözeri, H., S. E. Shirsath, S. Güner, S. Akhtar, & A. Manikandan, 'Impact of La^{3+} and Y^{3+} Ion Substitutions

.

on Structural, Magnetic and Microwave Properties of $Ni_{0.3}Cu_{0.3}Zn_{0.4}Fe_2O_4$ Nanospinel Ferrite Synthesized via Sonochemical Route', *RSC Advances* 9, 30671–30684, 2019.

3. K. Jangam, K. Patil, S. Balgude, S. Patange, & , P. More, 'Magnetically Separable $Zn_{1-x}Co_{0.5x}Mg_{0.5x}Fe_2O_4$ Ferrite: Stable and Efficient Sunlight-Driven Photocatalyst for Environmental Remediation' *RSC Advances*, 10, 42766–42776, 2020.
4. O. K. Nimisha, M. Akshay, S. Mannya, A. P. R. Mary, 'Synthesis and Photocatalytic Activity of Nickel Doped Zinc Ferrite', *Materials Today Proceedings* 66, 2370–2373, 2022.
5. N. I. Abu-Elsaad, A. S. Nawara, 'Effect of Cu Substitution on Magnetic and Photocatalytic Properties of Mn–$ZnFe_2O_4$ Nanoparticles', *Journal of Materials Science* 59, 4167–4185, 2024.
6. A. Nawaz, A. Khan, N. Ali, & M. Bilal, 'Fabrication and Characterization of New Ternary Ferrite-Chitosan Nanocomposite for Solar-Light Driven Photocatalytic Degradation of a Model Textile Dye', *Environmental Technology & Innovation*, 20, 101079–101079,2020.
7. R. Sharma, S. Bansal, S. Singhal, 'Tailoring the Photo-Fenton Activity of Spinel Ferrite (MFe_2O_4) by Incorporating Different Cations (M = Cu, Zn, Ni and Co) in the Structure', *RSC Advances*, 5, 6006–6018, 2014.
8. A. V. Bagade, S. N. Pund, P. A. Nagwade, B. Kumar, S. U. Deshmukh, A. B. Kanagare, 'Ni-Doped Mg-Zn Nano-Ferrite: Fabrication, Characterization, and Visible-Light-Driven Photocatalytic Degradation of Model Textile Dyes'. *Catalysis Communications*, 181, 106719–106719, 2023.
9. M. P. Gharehlar, S. Sheshmani, F. R. Nikmaram, Z. Doroudi, 'Synergistic Potential in Spinel Ferrite MFe_2O_4 (M = Co, Ni) Nanoparticles-Mediated Graphene Oxide: Structural Aspects, Photocatalytic, and Kinetic Studies'. *Scientific Report*, 14, 4625–4625, 2024.
10. C. Singh, A. Goyal, S. Singhal, 'Nickel-Doped Cobalt Ferrite Nanoparticles: Efficient Catalysts for the Reduction of Nitroaromatic Compounds and Photo-Oxidative Degradation of Toxic Dyes'. *Nanoscale*, 6, 7959–7970, 2014.
11. M. I. A. Abdel Maksoud, R. A. Fahim, A. G., Bedir, A. I. Osman, M. M. Abouelela, G. S. El-Sayyad, M. A. Elkodous, A. S. Mahmoud, M. M. Rabee, A. H. Al-Muhtaseb, D. W. Rooney,

.

'Engineered Magnetic Oxides Nanoparticles as Efficient Sorbents for Wastewater Remediation: A Review' *Environmental Chemistry Letters*, 20, 519–562, 2021.

12. B. Alqassem, F. Banat, G. Palmisano, M. A. Haija, 'Emerging Trends of Ferrite-Based Nanomaterials as Photocatalysts for Environmental Remediation: A Review and Synthetic Perspective', *Sustainable materials and technologies*, 40, 2024.
13. C. Celik, M. Yasar, K. J, Alzahrani, M. Abbas, S. Ganesan, A. Mujtaba, S. Mishra, J. Sharma, A, Sinha, F. M., 'Alzahrani, Synthesis, Characterization, and Mechanistic Insights into Enhanced Photocatalytic Tetracycline Degradation by Zinc-Doped Ferrite Nanoparticles', *Journal of Sol-Gel Science and Technology*, 117, 2026.
14. A. Azimi-Fouladi, P. Falak, S. A. Hassanzadeh-Tabrizi, 'The Photodegradation of Antibiotics on Nano Cubic Spinel Ferrite Photocatalytic Systems: A Review', *Journal of Alloys and Compounds*, 961, 171075–171075, 2023.
15. M. A. Almessiere, Y. Slimani, B. Ünal, T. I. Zubar, A. Sadaqat, A. Baykal, ' Microstructure, Dielectric and Microwave Features of $[Ni_{0.4}Cu_{0.2}Zn_{0.4}](Fe_{2-x}Tb)O_4$ ($x \leq 0.1$) Nanospinel Ferrite', *Journal of Materials Research and Technology*, 9, 10608–10623, 2020.
16. V. K. Sharma, C. He, R. Doong, D. D. Dionysiou, 'Water Depollution Using Ferrite Photocatalysts', *Environmental Chemistry for a Sustainable World*, 135–150, 2013.
17. A. Khan, Z. Valicsek, O. Horváth, M. M. Khan, A. Wafi, 'Ferrite-Based Photocatalysts: Synthesis, Modifications, and Key Parameters in Photocatalytic-Related Applications', *Materials Today Communications*, 40, 109556, 2024.
18. Md. N. Rahman, Md. A. Hossain, 'Transition Metal Based Spinel Ferrite: A Review', *Materials Today Sustainability*, 33, 101252, 2025.
19. B. B. Patil, 'A Review: Influence of Divalent, Trivalent, Rare Earth and Additives Ions on Ni–Cu–Zn Ferrite', *Journal of the Indian Chemical Society*, 100, 100811, 2022.
20. N. Shabelskaya, S. Sulima, E. Sulima, O. Medennikov, M. Kulikova, T. Kolesnikova, S. Sushkova, 'Study of the Possibility of Using Sol–Gel Technology to Obtain Magnetic Nanoparticles Based on Transition Metal Ferrite', *Gels*, 9, 217, 2023.

.

21. V. V. Awati, S. M. Rathod, M. L. Mane, K. C. Mohite, 'Influence of Zn^{2+} Doping on the Structural and Surface Morphological Properties of Nanocrystalline Ni–Cu Spinel Ferrite', *International Nano Letters*, 3, 2013.

22. T. Tangcharoen, A. Ruangphanit, W. Klysubun, W. Pecharapa, 'Characterization and Enhanced Photocatalytic Performance of Nanocrystalline Ni-Substituted Zn Ferrite Synthesized by DEA-Assisted Sol–Gel Auto-Combustion Method', *Journal of Sol-Gel Science and Technology*, 66, 387–398, 2013.

23. S. Diodati, R. I. Walton, S. Mascotto, S. Gross, 'Low-Temperature Wet Chemistry Synthetic Approaches towards Ferrite', *Inorganic Chemistry Frontiers*, 7, 3282–3314, 2020.

24. H. Hassen, M. Adel, Arbi, 'Effect of Pulsed and Continuous Ultrasound on Structural and Magnetic Properties of Nano-Sized $Ni_{0.4}Cu_{0.2}Zn_{0.4}Fe_2O_4$ Ferrite', *Journal of Alloys and Compounds*, 8, 723–728, 2018.

25. H. Harzali, F. Saida, A. Marzouki, A. Megriche, F. Baillon, F. Espitalier, A. Mgaidi, 'Structural and Magnetic Properties of Nano-Sized NiCuZn Ferrite Synthesized by Co-Precipitation Method with Ultrasound Irradiation', *Journal of Magnetism and Magnetic Materials*, 419, 50–56, 2016.

26. S. Dutta, M. Akhter, J. Ahmed, M. K. Amin, Palash, K. Dhar, 'Synthesis and Catalytic Activity of Spinel Ferrite: A Brief Review', *Biointerface Research in Applied Chemistry*, 12, 4399–4416, 2021.

27. V. V. Awati, K. Badave, D. Bobade, 'Effect of Tb^{3+} Substitution on Structural, Optical and Magnetic Properties of $NiCuZnFe_2O_4$ Prepared by Sol–Gel Route', *Indian Journal of Physics*, 96, 89–101, 2021.

28. A. E. Danks, S. R. Hall, Z. Schnepp, 'The Evolution of "Sol–Gel" Chemistry as a Technique for Materials Synthesis', *Materials Horizons*, 3, 91–112, 2015.

29. L.-Q. Gao, G. Yu, Y. Wang, F. Wei, 'Study of NiCuZn Ferrite Powders and Films Prepared by Sol–Gel Method', *Chinese Physics B*, 20, 027503, 2011.

30. A. Lassoued, M. S. Lassoued, B. Dkhil, S. Ammar, A. Gadri, 'Improved Photocatalytic Activities of $Cu_xCo_{0.5-x}Ni_{0.5}Fe_2O_4$ Nanoparticles through Co-Precipitation Method in

.

Degrading Methylene Blue', *Physica E: Low-Dimensional Systems and Nanostructures*, 101, 29–37, 2018.

31. T. S. Saleh, A. K. Badawi, R. S. Salama, M. M. M. Mostafa, 'Design and Development of Novel Composites Containing Nickel Ferrite Supported on Activated Carbon Derived from Agricultural Wastes and Its Application in Water Remediation', *Materials*, 16, 2170, 2023.
32. F. A. Hezam, N. O. Khalifa, O. Nur, M. A. Mustafa, 'Synthesis and Magnetic Properties of $Ni_{0.5}Mg_xZn_{0.5-x}Fe_2O_4$ ($0.0 \leq x \leq 0.5$) Nanocrystalline Spinel Ferrite', *Materials Chemistry and Physics*, 257, 123770, 2020.
33. O. H. Abuzeyad, A. M. El-Khawaga, M. A. Elsayed, 'Merits of Photocatalytic Activity of Synthesized ($Zn_xCu_{1-x}Fe_2O_4$; x = 0–1) Magnetic Nanoparticles for Wastewater Treatment', *Journal of Materials Science*, 59, 4152–4166, 2024.
34. E. M. Casbeer, V. K. Sharma, X. Li, 'Synthesis and Photocatalytic Activity of Ferrite under Visible Light: A Review', *Separation and Purification Technology*, 87, 1–14, 2011.
35. A. S. Al-Wasidi, E. A. Abdelrahman, K. ur Rehman, F. A. Saad, A. M. Munshi, 'Efficient Removal of Crystal Violet and Acid Red 88 Dyes from Aqueous Environments Using Easily Synthesized Copper Ferrite Nanoparticles', *Scientific Reports*, 14, 2024.
36. S. Lin, T. Zhang, 'Research Progress in Preparation and Application of Spinel-Type Metallic Oxides (M ≥ 2)', *Journal of Alloys and Compounds*, 962, 171117, 2023.
37. G. L. Mmethi, L. Mahlaule-Glory, N. Hintsho-Mbita, 'Progress in Green Metal Ferrite Nanoparticles as Photocatalysts for the Degradation of Dyes', *Next Materials*, 11, 101777, 2026.
38. N. K. Gupta, Y. Ghaffari, S. Kim, J. Bae, K. S. Kim, M. Saifuddin, 'Photocatalytic Degradation of Organic Pollutants over MFe_2O_4 (M = Co, Ni, Cu, Zn) Nanoparticles at Neutral pH', *Scientific Reports*, 10, 4942, 2020.
39. N. J. Mondal, R. Sonkar, B. Boro, M. P. Ghosh, D. Chowdhury, 'Nanocrystalline Ni–Zn Spinel Ferrite: Size-Dependent Physical, Photocatalytic and Antioxidant Properties', *Nanoscale Advances*, 5, 5460–5475, 2023.

.

40. J. Singh, A. S. Kalamdhad, J. R. Koduru, 'Potential Degradation of Hazardous Dye Congo Red by Nano-Metallic Particles Synthesized from the Automobile Shredder Residue', *Nanotechnology for Environmental Engineering*, 2–10, 2017.

41. J.-L. Ortiz-Quiñonez, U. Pal, M. S. Villanueva, 'Structural, Magnetic, and Catalytic Evaluation of Spinel Co, Ni, and Co–Ni Ferrite Nanoparticles Fabricated by Low-Temperature Solution Combustion Process', *ACS Omega*, 3, 14986–15001, 2018.

42. A. Farhan, J. Arshad, E. U. Rashid, H. Ahmad, S. Nawaz, J. Munawar, J. Zdarta, T. Jesionowski, M. Bilal, 'Metal Ferrite-Based Nanocomposites and Nanohybrids for Photocatalytic Water Treatment and Electrocatalytic Water Splitting', *Chemosphere*, 310, 136835, 2022.

43. P. O. Oladoye, M. O. Bamigboye, O. D. Ogunbiyi, M. T. Akano, 'Toxicity and Decontamination Strategies of Congo Red Dye', *Groundwater for Sustainable Development*, 19, 100844, 2022.

44. I. G. D. D. de Azevedo, M. A. Morales, C. P. de Souza, A. L. L. D. de Moriyama, 'Dyes Degradation Using Copper-Nickel Ferrite and Its Tunable Structural and Photocatalytic Properties', *Catalysts*, 14, 73, 2024.

45. Md. A. Kawsar, Md. S. Hossain, S. Tabassum, N. M. Bahadur, S. Ahmed, 'Synthesis of Different Types of Nano-Hydroxyapatites for Efficient Photocatalytic Degradation of Textile Dye (Congo Red): A Crystallographic Characterization', *RSC Advances*, 14, 11570–11583, 2024.

46. S. Rasheed, S. Nadeem, R. Nawaz, S. Razzaque, A. Mahmood, A. Zidan, W. Al-Masry, M. Javed, N. A. Ditta, A. Bahadur, S. Iqbal, S. Mahmood, T. Akhter, 'Revolutionizing Textile Wastewater Treatment: Enhanced Degradation of Dyes Using Bimetallic Zinc Ferrite-GO Nanocomposites', *Journal of Molecular Structure*, 1320, 139480, 2024.

47. B. Biswas, Md. F. Ahmed, L. Rahman, J. Khanam, Md. H. R. Bhuiyan, N. Sharmin, 'Investigation of Structural, Optical, and Magnetic Properties of $NiFe_2O_4$ for Efficient Photocatalytic Degradation of Organic Pollutants through Photo-Fenton Reactions', *Heliyon*, 10, e37199 , 2024.

.

48. H. Qin, Y. He, P. Xu, D. Huang, Z. Wang, H. Wang, W. Wang, Y. Zhao, Q. Tian, C. Wang, 'Spinel Ferrite (MFe_2O_4): Synthesis, Improvement and Catalytic Application in Environment and Energy Field', *Advances in Colloid and Interface Science*, 294, 102486, 2021.

49. A. Behera, D. Kandi, S. M. Majhi, S. Martha, K. Parida, 'Facile Synthesis of $ZnFe_2O_4$ Photocatalysts for Decolourization of Organic Dyes under Solar Irradiation', *Beilstein Journal of Nanotechnology*, 9, 436–446, 2018.

50. H. Kim, C. Park, N. Choi, K. Cho, 'Congo Red Dye Degradation Using Fe-Containing Mineral as a Reactive Material Derived from Waste Foundry Dust', *Environmental Science and Pollution Research*, 31, 28443–28453, 2024.

51. S. A. Jadhav, S. B. Somvanshi, M. V. Khedkar, S. R. Patade, K. M. Jadhav, 'Magneto-Structural and Photocatalytic Behavior of Mixed Ni–Zn Nano-Spinel Ferrite: Visible Light-Enabled Active Photodegradation of Rhodamine B', *Journal of Materials Science: Materials in Electronics*, 31, 11352–11365, 2020.

52. K. R. Krishna, D. Ravinder, K. V. Kumar, Ch. A. S. Lincon, 'Synthesis, XRD & SEM Studies of Zinc Substitution in Nickel Ferrites by Citrate Gel Technique', *World Journal of Condensed Matter Physics*, 2, 153–159, 2012.

53. Q. Yu, S. Yuchang, R. Tursun, J. Zhang, 'Synthesis and Characterization of Low-Density Porous Nickel Zinc Ferrites', *RSC Advances*, 9, 13173–13181, 2019.

54. A. Lucas, R. Lebourgeois, F. Mazaleyrat, É. Labouré, 'Temperature Dependence of Core Loss in Cobalt Substituted Ni–Zn–Cu Ferrites', *arXiv (Cornell University)*, 323, 735–739, 2010.

55. T. K. Bromho, K. Ibrahim, H. Kabir, M. M. Rahman, K. Hasan, T. Ferdous, H. Taha, M. Altarawneh, Z. Jiang, 'Understanding the Impacts of Al^{3+}-Substitutions on the Enhancement of Magnetic, Dielectric and Electrical Behaviors of Ceramic Processed Nickel-Zinc Mixed Ferrites: FTIR Assisted Studies', *Materials Research Bulletin*, 97, 444–451, 2017.

.